Journal of Theoretical and Applied Vibration and Acoustics 4(1) 99-124 (2018)

I S A V

Journal of Theoretical and Applied Vibration and Acoustics

journal homepage: http://tava.isav.ir

Transverse and longitudinal dynamic modeling of bimorph piezoelectric actuators with investigating the effect of vibrational modes

Mohamad Ebrahimi [a], **Hamed Ghafarirad** [a*], **Mohammad Zareinejad** [b]

[a] *Mechanical Engineering Department, Amirkabir University of Technology, Tehran, Iran*

[b] *New Technologies Research Centre, Amirkabir University of Technology, Tehran, Iran*

ARTICLE INFO

Article history:
Received 21 January 2018

Received in revised form
5 June 2018

Accepted 12 June 2018

Available online 15 June 2018

Keywords:
Bimorph piezoelectric actuator

Continuous modeling

Non-minimum phase system

Dynamic behavior analysis

Frequency response

ABSTRACT

Bimorph piezoelectric cantilevered (BPC) actuators have recently received a great deal of attention in a variety of micro-electromechanical systems (MEMS) applications. Dynamic modeling of such actuators needs to be improved in order to enhance the control performance. Previous works have usually taken transverse vibration into account without considering longitudinal vibration. This paper presents a comprehensive modeling for a set of transverse and longitudinal vibration equations for piezoelectric cantilevered actuators. In addition, dynamic behavior and exact non-minimum phase region along BPC is derived by analyzing first three vibrational modes. A simulation study is propounded to better analyze the system dynamic behavior. Finally, an experimental setup is developed to verify the proposed dynamic model. The modal frequency response of the system for the first three modes, obtained from the proposed model, is compared with those obtained from the experiment and a good consistency between them confirms the validity of the proposed dynamic model.

1. Introduction

Microcantilevers and cantilevers have emerged as efficacious tools for many nanomechanical sensing and actuating applications due to their simple structures and good maneuverability for transverse deflection. More specifically, piezoelectrically actuated micro-cantilevers such as

* Corresponding author:
E-mail address: Ghafarirad@aut.ac.ir (H. Ghafarirad)

http://dx.doi.org/10.22064/tava.2018.80223.1096

unimorph and bimorph piezoelectric cantilevers (BPC) have recently received considerable attention since they have unique features such as high natural frequency, fine working resolution and proper time response [1, 2], while also possessing self-sensing ability.

Applications of BPC structures can expand to several nano/micromechanical instruments mainly divided into two categories. With respect to their actuating effect, BPC actuators have been utilized in micro-manipulation applications such as cell characterization [3] and micro-assembly [4]. In addition, owing to their sensing effect, BPC structures have been used as various types of sensors including position sensors [5], force sensors [6], scanning force microscopy [7] and also energy harvester [8]. In dynamic mode of operation, a deep understanding of dynamic behavior of BPC actuator is essential, especially when it comes to choose an appropriate controller for real MEMS applications [9]. Several investigations have been conducted toward the subject with two main approaches; lumped and continuous modelling methods.

Considering lumped dynamic modelling method, a mass, spring and damper are utilized to model the cantilever dynamic behavior. Although this method has shown to be compatible for modeling two degree-of-freedom piezoelectric actuators [10], it has many limitations and could only be valid for specific target point on actuator [10]. While hysteresis effect can be modeled in this method by a nonlinear function [11], this method still is inefficacious for two main reasons. Firstly, the effect of higher vibrational modes on output response is ignored. Secondly, the effect of altering target point on dynamic behavior is not considered.

On the other hand, continuous dynamic modelling addresses the two drawbacks of lumped model. Bilgen *et al.* developed a model for dynamic behavior of a unimorph piezoelectric beam [12] which was improved to bimorph piezoelectric beam energy harvesters by Chen *et al.* [13]. Moreover, the dynamic model for BPC was considered based on Euler-Bernoulli and Timoshenko beam theory which pursue two main assumptions [14]. First, the effect of higher vibrational modes on the output dynamic behavior is neglected. Second, the dynamic model is considered to be linear which is because piezoelectric input voltage is assumed to be in a low-amplitude order then the nonlinear hysteresis effect on output dynamic response is considered to be negligible.

In some other works, effect of buffer layer and electrodes on output dynamic has been investigated [15] as well as effect of excitation frequency and actuator geometry [14]. In addition, effect of fringing fields at free end of beam is shown not to be negligible [16] and it was investigated for control applications [17]. Moreover, hysteresis effect was first added to linear dynamic model as a disturbance by Yi *et al.* [18] and it was improved by Chao *et al.* [19]. In these works, effect of higher vibrational modes and effect of target point position on BPC dynamic behavior were not considered. Ghafarirad *et al.* investigated the effect of higher modes up to second mode and also proposed a safe minimum phase region along the BPC based on position of actuator target point [20]. Moreover, the shear vibration modes for piezo laminated structures have been investigated by Tahmasebi *et al.* [21].

In this paper, the actuator transverse and longitudinal dynamic models have been analytically investigated. Furthermore, exact non-minimum phase region was extracted by analyzing the dynamic behavior of the system. Although in previous works the sufficient condition for non-minimum phase region was proposed [20], extracting exact non-minimum phase region is one the novelties of this paper. To investigate the effect of higher vibrational modes on output behavior, first three modes were considered for dynamic modelling of the BPC actuator as a case

study. Finally, the efficiency and accuracy of the proposed model were evaluated based on simulation and experimental results and an appropriate consistency between them was observed.

2. Transverse and longitudinal dynamic modeling

The case study in the current work will be conducted on a bimorph piezoelectric cantilevered (BPC) actuators with a rectangular cross section. Consider a piezo-layered cantilever with two piezoelectric patches on its top and beneath surfaces and a metallic bulk at the middle, as depicted in Figure 1.

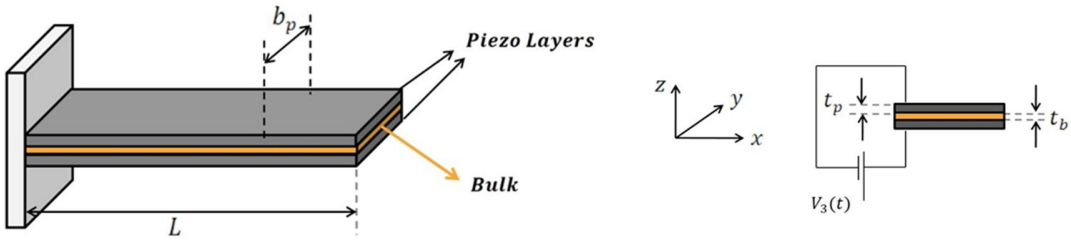

Fig. 1: Configuration of a BPC actuator

In order to model the dynamic behavior of the BPC actuator, it is assumed that the motion of BPC is governed by the Euler–Bernoulli theory, therefore shear deformation and rotary inertia terms are negligible. Based on this theory the dynamic behavior of a beam can be modeled as the following equations [22]:

Longitudinal vibration

$$\rho A_e \frac{\partial^2 u}{\partial t^2} = \frac{\partial N}{\partial x} \tag{1}$$

Transverse vibration

$$\rho A_e \frac{\partial^2 w}{\partial t^2} = \frac{\partial^2 M}{\partial x^2} - \frac{\partial}{\partial x}\left(N \frac{\partial w}{\partial x}\right) \tag{2}$$

where ρA_e denotes equivalent mass per unit length, N, and M represent internal longitudinal force and moment, while u and w represent displacement in x and z-direction, respectively. σ_1 is stress in x-direction, along the beam's length, and z denotes distance from neutral axis in vertical direction. Terms N and M can be obtained by integrating stress component over the beam's cross section as below formulations:

$$N = \int \sigma_1 \, dA \tag{3}$$

$$M = \int z \, \sigma_1 \, dA \tag{4}$$

In addition, regarding the Euler–Bernoulli beam theory, strain could be considered as a function of both transverse deflection and longitudinal displacement as:

$$S_1 = \frac{\partial u}{\partial x} - z \frac{\partial^2 w}{\partial x^2} \tag{5}$$

in which S_1 denotes strain in the x-direction. In this regard, neutral axis lies on the mid-plane of the beam due to geometrical symmetry.

For a piezoelectric material the stress formulation can be considered as [22]:

$$\sigma_{1,p} = C_p\, S_1 - e_{31}\, E_3 \tag{6}$$

C_p and e_{31} are elasticity modulus and piezoelectric constant, respectively. E_3 represents electric field in z-direction. A linear distribution for the electric field along the piezoelectric layer thickness (t_p) has been considered as [22]:

$$E_3 = \frac{V_3}{t_p} \tag{7}$$

where V_3 denotes exterior voltage. It's worth noticing that for a BPC actuator the polarization of the piezoelectric depends on the direction of the exterior electric field. For the BPC actuator configuration shown in Figure 1 the direction of electric field of the upper and lower piezoelectric layers oppose each other. Therefore, the redefinition of the stress relations could be as following equations:

$$\sigma_{1p,U} = C_p\, S_1 - e_{31}\, E_3 \tag{8}$$

$$\sigma_{1p,L} = C_p\, S_1 + e_{31}\, E_3 \tag{9}$$

The subscripts U and L represent upper and lower piezoelectric layers, respectively. Moreover, according to stress-strain relation for the bulk of the beam explained by Hook's law [23]:

$$\sigma_{1,b} = C_b\, S_1 \tag{10}$$

Subscripts p and b denote piezoelectric layers and beam bulk, respectively. Also t_b denotes beam's bulk thickness. Note that the beam bulk and piezoelectric layers have same width which has been denoted by symbol Y. It is also worth mentioning the following relations regarding cross sectional area:

$$\int zdA = \int_{-r}^{r} zYdz = 0 \qquad \int_{\frac{-t_b}{2}}^{\frac{t_b}{2}} z^2 Ydz = \frac{Y\, {t_b}^3}{12} = I_b$$
$$\int_{\frac{t_b}{2}}^{\left(\frac{t_b}{2}+t_p\right)} z^2 Ydz + \int_{-\left(\frac{t_b}{2}+t_p\right)}^{\frac{-t_b}{2}} z^2 Ydz = \frac{Y\left(\left(2t_p + t_b\right)^3 - {t_b}^3\right)}{12} = I_p \tag{11}$$

In order to complete the formulation of beam's vibration, it is necessary to derive terms N and M as functions of displacement terms i.e. u and w. This is done by substituting equations (5) to (10) into (3) and (4) as followings:

$$N = \int_{\frac{-t_b}{2}}^{\frac{t_b}{2}} C_b\, S_1 Ydz + \int_{\frac{t_b}{2}}^{\left(\frac{t_b}{2}+t_p\right)} (C_p\, S_1 - e_{31}\, E_3) Ydz + \int_{-\left(\frac{t_b}{2}+t_p\right)}^{\frac{-t_b}{2}} (C_p\, S_1 + e_{31}\, E_3)\, Ydz$$
$$= (C_b A_b + C_p A_p)\frac{\partial u}{\partial \mathrm{x}} \tag{12}$$

$$M = \int_{\frac{-t_b}{2}}^{\frac{t_b}{2}} zC_b\, S_1 Y dz + \int_{\frac{t_b}{2}}^{\left(\frac{t_b}{2}+t_p\right)} z(C_p\, S_1 - e_{31}\, E_3) Y dz + \int_{-\left(\frac{t_b}{2}+t_p\right)}^{\frac{-t_b}{2}} z(C_p\, S_1 + e_{31}\, E_3)\, Y dz$$
$$= -(C_b I_b + C_p I_p)\frac{\partial^2 w}{\partial x^2} - \left(t_b + t_p\right) Y e_{31} V_3(t) \tag{13}$$

Finally, the total internal longitudinal force and moment can be calculated as:

$$N = CA_e \frac{\partial u}{\partial x} \tag{14}$$

$$M = -CI_e \frac{\partial^2 w}{\partial x^2} - M_p V_3(t) G(x) \tag{15}$$

where CA_e and CI_e are effective axial and bending rigidity, respectively, and can be expressed as $CA_e = C_b A_b + C_p A_p$ and $CI_e = C_b I_b + C_p I_p$. Aforementioned $M_p V_3(t)$ refers to bending moment due to piezoelectric electromechanical reaction to external voltage where M_p

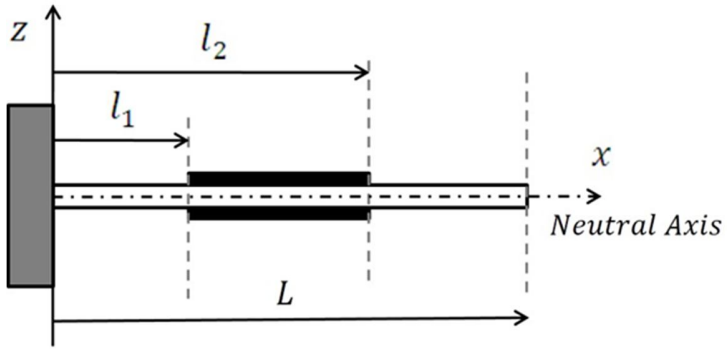

Fig. 2: Piezoelectric patch along the beam

can be calculated as $M_p = \left(t_b + t_p\right) Y e_{31}$.

It should be noted that $G(x)$ represents location of the piezoelectric patch along the beam. Considering the Figure 2, a general notation for this function is: $G(x) = H(x - l_1) - H(x - l_2)$ where $H(x)$ is the *Heaviside* function which is defined as: $H(x) = \int_0^x \delta(s) ds$ or $\delta(x) = \frac{\partial H(x)}{\partial x}$ where $\delta(x)$ denotes the *Dirac* delta function [24]. l_1 and l_2 represent starting and ending point of the piezoelectric patch, respectively. In the current case study both the top and beneath piezoelectric layers lie on whole length of the beam therefore $l_1 = 0$ and $l_2 = L$ thus $G(x)$ could be simplified as $G(x) = -H(x - L)$.

Now, by substituting (14) and (15) into (1) and (2), assuming that geometrical and mechanical properties will remain constant along the beam, governing coupled longitudinal and transverse vibration equations of BPC would be:

$$\rho A_e \frac{\partial^2 u}{\partial t^2} = \frac{\partial}{\partial x}\left(CA_e \frac{\partial u}{\partial x}\right) \tag{16}$$

$$\rho A_e \frac{\partial^2 w}{\partial t^2} = -\frac{\partial^2}{\partial x^2}\left(CI_e \frac{\partial^2 w}{\partial x^2}\right) - M_p V_3 \frac{\partial^2 G(x)}{\partial x^2} - \frac{\partial}{\partial x}\left(CA_e \frac{\partial u}{\partial x}\frac{\partial w}{\partial x}\right) \tag{17}$$

where ρA_e represents equivalent mass per unit length of the beam and is equal to $\rho_b A_b + \rho_p A_p$.

Symmetry in BPC geometry eliminates the effect of transverse vibration in longitudinal vibration equation, while difference in polarization direction in piezoelectric layers eliminates the effect of external voltage in the longitudinal vibration equation. Overall, the only remained nonlinear effect is the effect of longitudinal vibration on transverse vibration equation. So, the dynamic is simplified and coupling is considered as a weak type of coupling which has been eliminated in previous researches [25-27].

Also, the effect of axial force caused by longitudinal elastic strain could be considered negligible in transverse vibration [23]. So, it is possible to neglect the effect of longitudinal vibration on transverse vibration which leads to an uncoupled equation for transverse vibration as:

$$\rho A_e \frac{\partial^2 w}{\partial t^2} = -\frac{\partial^2}{\partial x^2}\left(CI_e \frac{\partial^2 w}{\partial x^2}\right) - M_p V_3 \frac{\partial^2 G(x)}{\partial x^2} \tag{18}$$

As a BPC actuator vibrates in an air environment, it interacts with surrounding air molecules and will cause an air flow. Thus, a hydrodynamic force will be exerted on the beam which results damping effects on the system. In addition, there is always inevitable structural damping which occurs due to strain rate [28]. Neglecting all other sorts of damping, the vibration equations could be modified as followings:

$$\rho A_e \frac{\partial^2 u}{\partial t^2} + B_{au} \frac{\partial u}{\partial t} - \frac{\partial}{\partial x}\left(B_{su} \frac{\partial^2 u}{\partial x \partial t}\right) - \frac{\partial}{\partial x}\left(CA_e \frac{\partial u}{\partial x}\right) = 0 \tag{19}$$

$$\rho A_e \frac{\partial^2 w}{\partial t^2} + B_{aw} \frac{\partial w}{\partial t} + \frac{\partial^2}{\partial x^2}\left(B_{sw} \frac{\partial^3 w}{\partial x^2 \partial t}\right) + \frac{\partial^2}{\partial x^2}\left(CI_e \frac{\partial^2 w}{\partial x^2}\right) = -M_p V_3 \frac{\partial^2 G(x)}{\partial x^2} \tag{20}$$

B_a and B_s represent the coefficients of viscous damping in air and structural damping, respectively. Subscripts u and w denote longitudinal and transverse domains, respectively.

2.1. Dynamic model discretization

In this section, a solution for the derived vibration equations is achieved by discretizing the continuous dynamic model. To discretize the continuous dynamic model, the separation of variables technique is utilized. Since the vibration equations are considered to be decoupled according to section 2.1, exact solution, with respect to length variable (x), is obtained for both vibration equations by satisfying all boundary conditions and applying exact mode shapes.

2.1.1. Longitudinal dynamic model discretization

The longitudinal displacement $u(x,t)$ can be expressed by a uniform convergent series of *eigen-functions* as [23]:

$$u(x,t) = \sum_{i=1}^{n} D_i \theta_i(x) \eta_i(t) \tag{21}$$

where $\theta_i(x)$ represents exact un-damped mode shapes which could be calculated by satisfying the boundary conditions. D_i is mode shape normalizing coefficient which is further defined in (27). Considering the cantilever in Figure 1, boundary conditions could be as:

$$u(x,t)|_{x=0} = 0 \qquad \forall i:\ \theta_i(x)|_{x=0} = 0$$
$$N|_{x=L} = CA_e \frac{\partial u(x,t)}{\partial x}\Big|_{x=L} = 0 \qquad \forall i:\ \frac{\partial \theta_i(x)}{\partial x}\Big|_{x=L} = 0 \tag{22}$$

To satisfy the above boundary conditions, exact solution for $\theta_i(x)$ is [23]:

$$\theta_i(x) = \mathrm{Sin}[(2i-1)\frac{\pi x}{2L}] \tag{23}$$

The most important feature of mode shapes is their orthogonality which could be expressed as following equations utilizing *Kronecker* delta function [23]:

$$\int_0^L \rho A_e D_m \theta_m(x)\, D_n \theta_n(x) dx = \kappa_{mn} \tag{24}$$

$$\int_0^L D_m \theta_m(x) \frac{\partial}{\partial x}(CA_e \frac{\partial (D_n \theta_n(x))}{\partial x}) dx = -\omega_{um}^2\, \kappa_{mn} \tag{25}$$

κ_{mn} denotes the *Kronecker* delta function which is defined as $\kappa_{mn} = \begin{cases} 1 & m = n \\ 0 & m \neq n \end{cases}$ and ω_{ui} represents the *i*-th undamped natural frequency of longitudinal vibration. Substituting (21) into (16), assuming all mode shapes at the same vibrating frequency ($\bar{u}_i(x,t) = \theta_i(x)e^{i\omega t}$) will lead to a formula for calculating undamped natural frequencies as:

$$\omega_{ui} = (2i-1)\frac{\pi}{2L}\sqrt{\frac{CA_e}{\rho A_e}} \tag{26}$$

Considering (24) and assuming m and n denote the same mode shape, then D_i will be defined as:

$$\int_0^L \rho A_e D_i \theta_i(x)\, D_i \theta_i(x) dx = 1 \ \rightarrow D_i = \frac{1}{\sqrt{\int_0^L \rho A_e {\theta_i}^2(x) dx}} \tag{27}$$

To discretize the continuous longitudinal vibration, (21) is substituted in (19):

$$\rho A_e \sum_{i=1}^{n} D_i \theta_i(x) \frac{\partial^2 \eta_i(t)}{\partial t^2} + B_{au} \sum_{i=1}^{n} D_i \theta_i(x) \frac{\partial \eta_i(t)}{\partial t} - \frac{\partial}{\partial x}(B_{su} \sum_{i=1}^{n} D_i \frac{\partial \theta_i(x)}{\partial x} \frac{\partial \eta_i(t)}{\partial t}) - \frac{\partial}{\partial x}(CA_e \sum_{i=1}^{n} D_i \frac{\partial \theta_i(x)}{\partial x}) \eta_i(t) = 0 \tag{28}$$

Multiplying $D_j \theta_j(x)$ to this equation and integrating along the beam and utilizing (24) and (25) will lead to final discretized equation for longitudinal vibration:

$$\ddot{\eta}_\iota + (\alpha_u + \beta_u \omega_{ui}^2)\dot{\eta}_\iota + \omega_{ui}^2 \eta_i = 0 \tag{29}$$

where α_u, β_u are proportional damping coefficients that can be identified only by experiment and are constant for each actuator [29]. B_{au} and B_{su} are generally complicated functions since they are affected by many parameters but in our cases study they are considered to be constant which is justifiable by assuming constant geometry and mechanical properties along the cantilever and also a relatively stable environmental condition.

$$\alpha_u = \int_0^L B_{au} D_i \theta_i(x) D_j \theta_j(x) dx = \frac{B_{au}}{\rho A_e} \kappa_{ij} \tag{30}$$

$$\beta_u = \int_0^L \frac{\partial}{\partial x}\left(B_{su} D_i \frac{\partial \theta_i(x)}{\partial x}\right) D_j \theta_j(x) dx = -\frac{B_{su}}{C A_e} \omega_{ui}^2 \kappa_{ij} \tag{31}$$

2. 1.2. Transvers dynamic model discretization

Similar to longitudinal displacement, transverse displacement $w(x,t)$ can also be expressed by a uniformly convergent series of *eigen-functions* as [23]:

$$w(x,t) = \sum_{i=1}^{n} K_i \varphi_i(x) \xi_i(t) \tag{32}$$

Where $\varphi_i(x)$ denotes exact un-damped mode shapes which could be calculated by satisfying the boundary conditions. K_i is mode shape normalizing coefficient which is further defined in (40). For a cantilevered beam in Figure 1 by considering that exact mode shapes are expressed as: $\varphi_i(x)=A_1 Cos(\gamma_i x) + A_2 Sin(\gamma_i x) + A_3 Cosh(\gamma_i x) + A_4 Sinh(\gamma_i x)$, the coefficients A_1, A_2, A_3, A_4 could be determined by satisfying the boundary conditions as the following formulation. Note that shear force (Q) acting on a beam is equal to $Q = CI_e \frac{\partial^3 w}{\partial x^3}$ according to Euler–Bernoulli beam's theory.

$$\begin{aligned}
&w(x,t)|_{x=0} = 0 && M|_{x=L} = -CI_e \left.\frac{\partial^2 w(x,t)}{\partial x^2}\right|_{x=L} = 0 \\
&\left.\frac{\partial w(x,t)}{\partial x}\right|_{x=0} = 0 && \forall i: \left.\frac{\partial \varphi_i(x)}{\partial x}\right|_{x=0} = 0 \\
&Q|_{x=L} = CI_e \left.\frac{\partial^3 w(x,t)}{\partial x^3}\right|_{x=L} = 0 && \forall i: \left.\frac{\partial^3 \varphi_i(x)}{\partial x^3}\right|_{x=L} = 0 \\
&M|_{x=L} = -CI_e \left.\frac{\partial^2 w(x,t)}{\partial x^2}\right|_{x=L} = 0 && \forall i: \left.\frac{\partial^2 \varphi_i(x)}{\partial x^2}\right|_{x=L} = 0
\end{aligned} \tag{33}$$

Substituting the assumed $\varphi_i(x)$ in the above boundary conditions leads to frequency equation and below alleviations:

Frequency Equation: $$\forall i: Cos(\gamma_i L)\, Cosh(\gamma_i L) = -1 \tag{34}$$

Alleviations: $$\forall i: \begin{cases} A_1 = A_3 = 0 \\ A_4 = -\dfrac{Cos(\gamma_i L) + Cosh(\gamma_i L)}{Sin(\gamma_i L) + Sinh(\gamma_i L)} A_2 \end{cases} \tag{35}$$

And hence the *i*th mode shape can be expressed as:

$$\varphi_i(x) = [Cos(\gamma_i x) - Cosh(\gamma_i x)] - \frac{Cos(\gamma_i L) + Cosh(\gamma_i L)}{Sin(\gamma_i L) + Sinh(\gamma_i L)} [Sin(\gamma_i x) - Sinh(\gamma_i x)] \tag{36}$$

Orthogonality of mode shapes for the transverse vibration would result [23]:

$$\int_0^L \rho A_e K_m \varphi_m(x)\, K_n \varphi_n(x) dx = \kappa_{mn} \tag{37}$$

$$\int_0^L K_m \varphi_m(x) \frac{\partial^2}{\partial x^2} (CI_e \frac{\partial^2 (K_n \varphi_n(x))}{\partial x^2}) dx = \omega_m^2 \kappa_{mn} \tag{38}$$

where ω_{wi} represents the *i*th un-damped natural frequency. Substituting (32) into (18), assuming all mode shapes at the same vibrating frequency ($\overline{w}_i(x,t) = \varphi_i(x)e^{i\omega t}$) and no external perturbations ($M_p V_3 = 0$), will lead to the definition of undamped natural frequency as:

$$\omega_{wi} = {\gamma_i}^2 \sqrt{\frac{CI_e}{\rho A_e}} \tag{39}$$

Where γ_i could be obtained by solving the frequency equation (34) numerically and the results are $\gamma_i L = \{1.875\ , 4.694\ , 7.855\ , 10.995\ , \ldots.\}$ that accounts for different mode shapes.

Considering (32) and assuming the same mode shapes, then K_i will be derived as:

$$\int_0^L \rho A_e K_i \varphi_i(x)\, K_i \varphi_i(x) dx = 1 \ \rightarrow K_i = \frac{1}{\sqrt{\int_0^L \rho A_e {\varphi_i}^2(x) dx}} \tag{40}$$

To discretize the continuous transverse vibration, (32) is substituted in (20):

$$\begin{aligned} \rho A_e \sum_{i=1}^{n} K_i \varphi_i(x) \frac{\partial^2 \xi_i(t)}{\partial t^2} + B_{aw} \sum_{i=1}^{n} K_i \varphi_i(x) \frac{\partial \xi_i(t)}{\partial t} + \frac{\partial^2}{\partial x^2}\left(B_{sw} \sum_{i=1}^{n} K_i \frac{\partial^2 \varphi_i(x)}{\partial x} \frac{\partial \xi_i(t)}{\partial t}\right) \\ + \frac{\partial^2}{\partial x^2}\left(CI_e \sum_{i=1}^{n} K_i \frac{\partial \varphi_i(x)}{\partial x}\right)\xi_i(t) = -M_p V_3 \frac{\partial^2 G(x)}{\partial x^2} \end{aligned} \tag{41}$$

it should change to 37 according to Q4

Multiplying $K_j \varphi_j(x)$ to this equation and integrating along the beam and substituting (37) and (38) in (41) will lead the formulation to the discretized transverse vibration equation:

$$\ddot{\xi}_\iota + (\alpha_w + \beta_w \omega_{wi}^2)\dot{\xi}_\iota + \omega_{wi}^2 \xi_i = -M_p V_3 \int_0^L K_j \varphi_j(x) \frac{\partial^2 G(x)}{\partial x^2} dx \tag{42}$$

Where α_w , β_w are proportional damping coefficients that can be identified only by experiment and are constant for each actuator [29]. For similar reasons mentioned in section 2.2.1 B_{aw} and B_{sw} are considered constant values in our case study; hence, α_w , β_w could be defined as:

$$\alpha_w = \int_0^L B_{aw} K_i \varphi_i(x) K_j \varphi_j(x) dx = \frac{B_{aw}}{\rho A_e}\, \kappa_{ij} \tag{43}$$

$$\alpha_w = \int_0^L B_{aw} K_i \varphi_i(x) K_j \varphi_j(x) dx = \frac{B_{aw}}{\rho A_e}\, \kappa_{ij} \tag{44}$$

To put forward (39), since $G(x) = -H(x-L)$ and $\delta(x-L) = \frac{\partial H(x-L)}{\partial x}$, thus $\frac{\partial^2 G(x)}{\partial x^2} = -\frac{\partial \delta(x-L)}{\partial x}$ and the aforementioned *Dirac* delta function will be utilized to simplify right-hand side of the equation. For any arbitrary target point l_t $(0 < l_t < L)$:

$$\int_0^L \varphi_j(x) \frac{\partial \delta(x-l_t)}{\partial x} dx = -\int_0^L \frac{\partial \varphi_j(x)}{\partial x} \delta(x-l_t) dx = -\left.\frac{\partial \varphi_j(x)}{\partial x}\right|_{x=l_t} \tag{45}$$

Now, by substituting (42) to (39):

$$\ddot{\xi}_\iota + (\alpha_w + \beta_w \omega_{wi}^2)\dot{\xi}_\iota + \omega_{wi}^2 \xi_i = -M_p V_3 K_i \left.\frac{\partial \varphi_i(x)}{\partial x}\right|_{x=L} \tag{46}$$

Note that V_3 is the key factor that runs the actuator and since it's an external input to the plant, generally it is considered as function of time $V_3 = V_3(t)$ and for further simplifications in notations: $m_{pi} = -M_p K_i \frac{\partial \varphi_i(x)}{\partial x}\Big|_{x=L}$, $2\mu_i\omega_{wi} = \alpha_w + \beta_w\omega_{wi}^2$ where μ_i is linear damping coefficient of the system and should be identified experimentally for at least two vibrational modes. Then α_w, β_w and damping coefficients B_{aw}, B_{sw} could readily be calculated using:

$$\begin{bmatrix}\alpha_w \\ \beta_w\end{bmatrix} = \begin{bmatrix}1 & \omega_{wi}^2 \\ 1 & \omega_{wj}^2\end{bmatrix}^{-1} \begin{bmatrix}2\mu_i\omega_{wi} \\ 2\mu_j\omega_{wj}\end{bmatrix} \tag{47}$$

3. Analysis of dynamic behavior

In this section, dynamic behavior of a BPC actuators is investigated. In the previously presented models, only first two vibrational modes were considered and only sufficient non-minimum phase region has been identified, but here we identify exact non-minimum phase region along the actuator's length. Also, in the previous researches only first two vibrational modes have been investigated but here we consider first three modes and show how considering the third mode will change the minimum phase region.

A linear dynamic system is called minimum phase if all of its transfer function zeroes are located in the left half plane (LHP). If the transfer function includes any right half plane (RHP) zero, the system would be non-minimum phase [30, 31].

The concept of non-minimum phase dynamic plays a paramount important role in control micro-manipulation processes and that is because a non-minimum phase system may lead to instability in control of such systems [30]. Thus, the conditions causing a dynamic system such as a BPC to be a non-minimum phase system and also vulnerability of such system to become a non-minimum system should be precisely determined.

For an arbitrary target point on the beam (l_t), transverse deflection according to first three mode shapes could be represented as: $w(x,t) = K_1\varphi_1(x)\xi_1(t) + K_2\varphi_2(x)\xi_2(t) + K_3\varphi_3(x)\xi_3(t)$. Different mode shapes could be visualized as Figure 3.

Considering $V_3(t)$ and $w(x,t)$ as the input and output of the control plant, respectively, for any arbitrary target point (l_t) transfer function $T(s)$ could be driven from (46) as:

$$T(s) = \frac{w(l_t)}{V_3} = \frac{m_{p1}\varphi_1(l_t)}{s^2 + 2\mu_1\omega_{w1}s + \omega_{w1}^2} + \frac{m_{p2}\varphi_2(l_t)}{s^2 + 2\mu_1\omega_{w1}s + \omega_{w2}^2} + \frac{m_{p3}\varphi_3(l_t)}{s^2 + 2\mu_1\omega_{w1}s + \omega_{w3}^2} = \frac{N(s)}{D(s)} \tag{48}$$

Where $N(s)$ and $D(s)$ are the numerator and denominator of the transfer function, respectively. It should be noted that due to the definition of m_{pi} , its sign is the same as the sign of $\frac{\partial \varphi_i(x)}{\partial x}\Big|_{x=L}$; thus, for example, $m_{p1} > 0$ according to Figure 3 first mode shape.

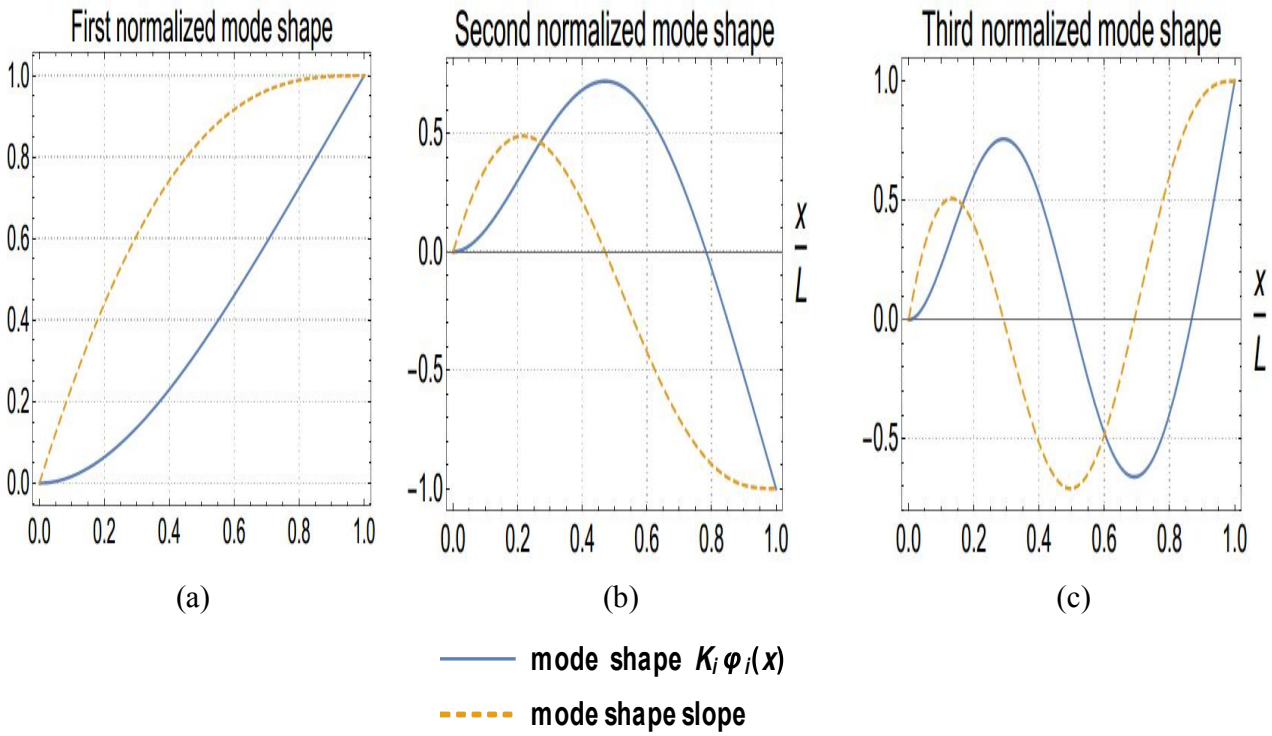

Fig. 3: First three mode shapes of a length-normalized BPC actuator
(a) First Mode, (b) Second Mode, (c) Third Mode

The location of the zeroes deeply impresses the stability of the plant as well as its dynamic behavior in the closed-loop system. Analyzing roots of $N(s)$ would give us the zeros of the system:

$$N(s) = m_{p1}\varphi_1(l_t)[a_1 s^4 + a_2 s^3 + a_3 s^2 + a_4 s^1 + a_5] \tag{49}$$

$$a_1 = 1 + \lambda_2 + \lambda_3 \qquad \lambda_2 = \frac{m_{p2}\varphi_2(l_t)}{m_{p1}\varphi_1(l_t)} \qquad \lambda_3 = \frac{m_{p3}\varphi_3(l_t)}{m_{p1}\varphi_1(l_t)},$$

$$\begin{aligned} a_2 &= (2\mu_2\omega_{w2} + 2\mu_3\omega_{w3}) + \lambda_2(2\mu_1\omega_{w1} + 2\mu_3\omega_{w3}) + \lambda_3(2\mu_1\omega_{w1} + 2\mu_2\omega_{w2}) \\ a_3 &= (\omega_{w2}^2 + \omega_{w3}^2 + 4\mu_2\omega_{w2}\mu_3\omega_{w3}) + \lambda_2(\omega_{w1}^2 + \omega_{w3}^2 + 4\mu_1\omega_{w1}\mu_3\omega_{w3}) \\ &\quad + \lambda_3(\omega_{w1}^2 + \omega_{w2}^2 + 4\mu_1\omega_{w1}\mu_2\omega_{w2}), \\ a_4 &= (2\mu_2\omega_{w2}\omega_{w3}^2 + 2\mu_3\omega_{w3}\omega_{w2}^2) + \lambda_2(2\mu_1\omega_{w1}\omega_{w3}^2 + 2\mu_3\omega_{w3}\omega_{w1}^2) \\ &\quad + \lambda_3(2\mu_1\omega_{w1}\omega_{w2}^2 + 2\mu_2\omega_{w2}\omega_{w1}^2), \\ a_5 &= (\omega_{w2}^2\omega_{w3}^2) + \lambda_2(\omega_{w1}^2\omega_{w3}^2) + \lambda_3(\omega_{w1}^2\omega_{w2}^2) \end{aligned} \tag{50}$$

To have the system remaining in the minimum phase region, it is necessary to locate all of zeroes in LHR region. It also should be noticed that $m_{p1}\varphi_1(l_t) > 0$ is valid for any arbitrary target point (l_t). Thus, the sufficient prerequisite condition for minimum phase region is [30]:

$$S1 = s_1 + s_2 + s_3 + s_4 = \frac{-a_2}{a_1} < 0$$
$$S2 = s_1s_2 + s_1s_3 + s_1s_4 + s_2s_3 + s_2s_4 + s_3s_4 = \frac{a_3}{a_1} > 0$$
$$S3 = s_1s_2s_3 + s_1s_2s_4 + s_1s_3s_4 + s_2s_3s_4 = \frac{-a_4}{a_1} < 0 \quad (51)$$
$$S4 = s_1s_2s_3s_4 = \frac{a_5}{a_1} > 0$$

where s_1, s_2, s_3, s_4 represent the zeros of $N(s)$. Moreover, the sufficient prerequisite condition to have all four zeroes in the LHR region is: $S1, S3 < 0$ and $S2, S4 > 0$. It is obvious that the recent condition only depends on magnitude and sign of the λ_2 , λ_3. One of the sufficient conditions that provides the system with minimum phase region is when: $a_1, a_2, a_3, a_4, a_5 > 0$ or when: λ_2 , $\lambda_3 > 0$ which is attained, according to Figure 3, if the target point is to be located after the second node of the third mode shape ($x > 0.868L$). That's because in this region $m_{p2} < 0$, $\varphi_2(l_t) < 0$ and also $m_{p3} > 0$, $\varphi_3(l_t) > 0$; thus, the result would be: $\lambda_2 > 0$ and $\lambda_3 > 0$. Figure 4 shows the specified region.

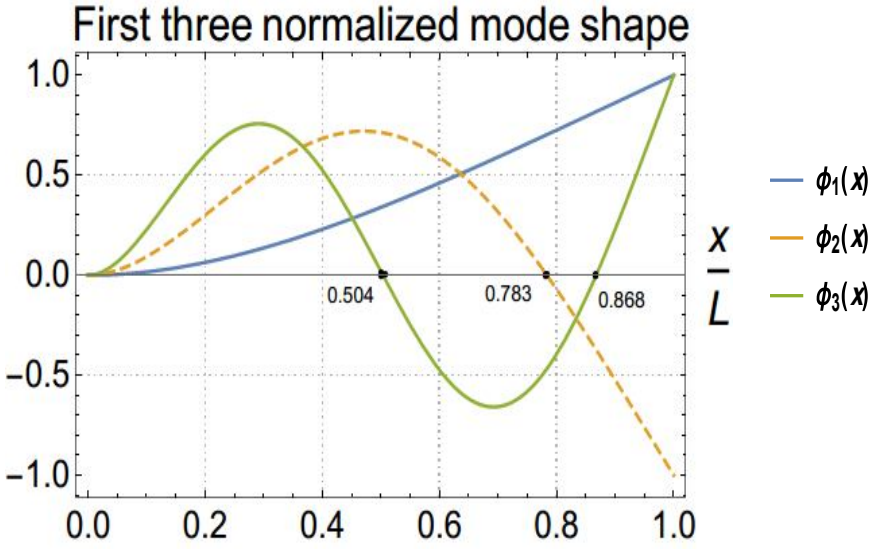

Fig. 4: First three mode shapes of a length-normalized BPC actuator. Target point at x > 0.868L provides the system a sufficient condition for minimum phase criteria

Following same procedure for only first two mode shapes would result in x > 0.783L as a condition that provides the system with minimum phase region. This means that once we consider the third mode in addition to first two mode shapes, the minimum phase region shrinks i.e. moves from node of the second mode shape to last node of the third mode shape. So, the more mode shapes we consider the smaller the minimum phase region becomes and the last node of the highest mode shape defines the minimum phase region.

In next step, exact edge of minimum phase criteria will be investigated. Finding the border of minimum phase and non-minimum phase region is important since it's decisive for determining

safety factor when it comes to design a controller for BPC actuators. According to aforementioned conditions for minimum phase region, both $S1, S3 < 0$ and $S2, S4 > 0$ must be satisfied simultaneously. $S1, S2, S3, S4$ are obtained by substituting (50) into (51) and are depicted a function over cantilever's length.

As it is seen in Figure 5, the region over the beam that satisfies $S1, S3 < 0$ and $S2, S4 > 0$ simultaneously is when target point is located at $x > 0.868L$. Conclusively, the edge of minimum and non-minimum phase region is $x = 0.868L$ when first three mode shapes are taken into consideration which is located before the second node of the third mode shape.

Same conclusion could be made based on Figure 6 which is the plot for a_1 to a_5:

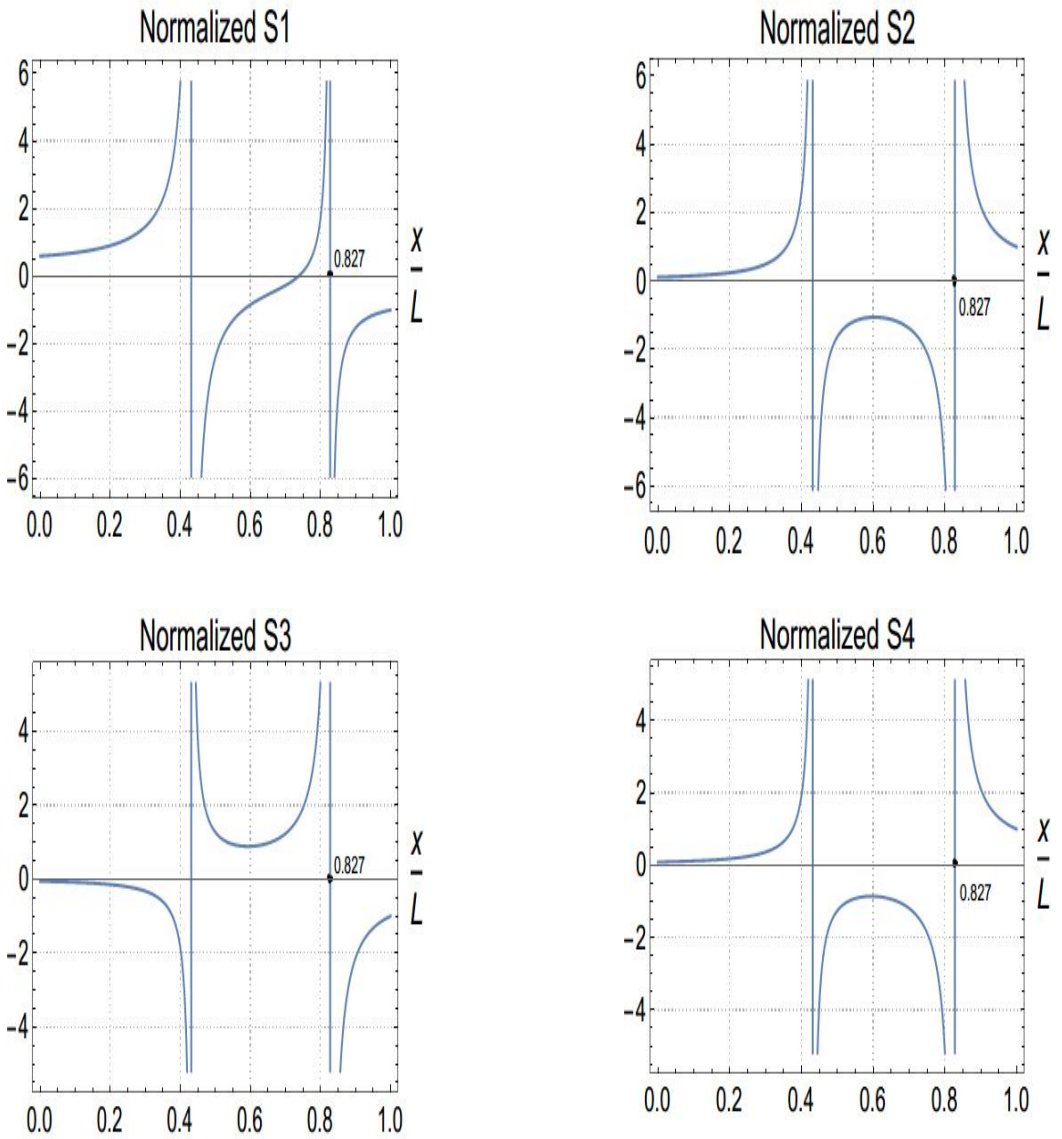

Fig. 5: Normalized $S1, S2, S3, S4$ for a BPC actuator, considering first three mode shapes

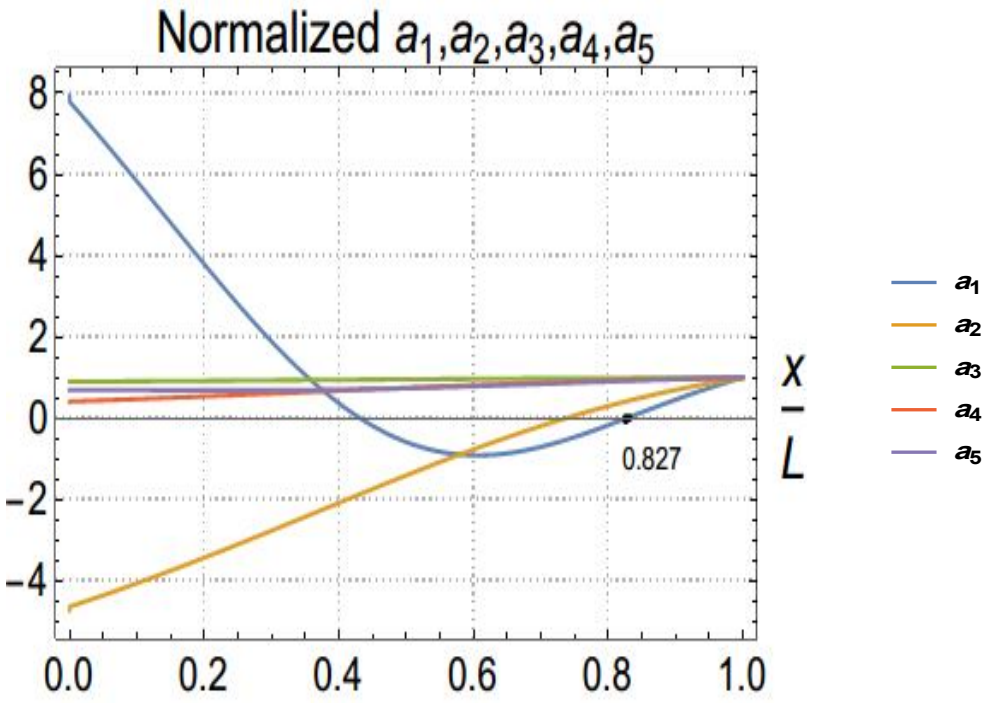

Fig. 6: Normalized a_1 *to* a_5 for a BPC actuator, considering first three mode

As it is seen from Figure 6, if the target point is located at $x > 0.868L$, the cantilever's dynamic system is considered minimum phase.

3.1. Simulation study for dynamic behavior analysis

A case study is done to investigate the consistency and accuracy of the proposed analytical analysis. In this regard, a cantilever made of brass and fully covered by piezoelectric layers on both sides, is considered dynamic system for case study. The material properties of the Brass substrate and PZT layers are shown in Table 1. Note that piezoelectric material for this cases study is PZT-5A.

It should be noted that α_w and β_w are damping coefficients that are calculated using experimental results and the process is further explained in section 4.1. Damping coefficients are considered unique for the whole system so the values of these parameters are considered the same for bulk substrate and piezoelectric layers. Moreover, according to considered material properties, first three natural frequencies are attained according to (39) and listed in Table 2.

Zero-elimination phenomenon happens here by changing from minimum phase to non-minimum phase region along the cantilever i.e. RHP zeroes appear in the cantilever's dynamic system by changing the target point. To elaborate on that, Bode magnitude plot and frequency response of the cantilever for three target points including $0.9L$ and $0.8L$ and $0.7L$ are shown in Figure 7 and Figure 8, respectively. Moreover, root locus analysis, shown in Figure 9 and Figure 10, help to picture how zeros appear in RHP when dynamic system becomes non-minimum phase.

Table 1: Material properties of Brass substrate and piezoelectric layers used in BPC

Symbol		Unit	PZT-5A	Brass
Y	Width	(mm)	3	3
L	Length	(mm)	23.98	23.98
t_b , t_p	Thickness	(mm)	0.13 (each)	0.12
ρ	Mass density	(kg/m^3)	7800	9000
C_b , C_p	Modules of elasticity	(G Pa)	58	105
e_{31}	Piezoelectric constant	(C/m^2)	-5.7	----
α_w	Mass damping coefficients	----	1e-4	
β_w	Stiffness damping coefficient	----	1e-6	
μ_1	1st Linear damping coefficient	----	8.6e-4	
μ_2	2nd Linear damping coefficient	----	5.4e-3	

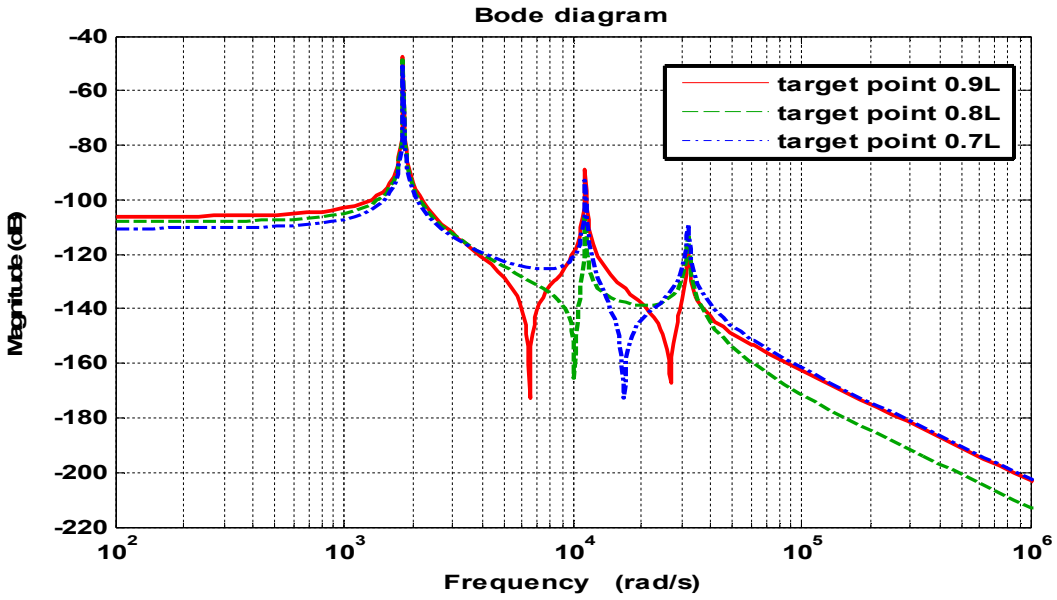

Fig. 7: Bode magnitude plot for different target points on the cantilever

Table 2: First three natural frequencies of the BPC actuator

Mode number	Natural frequency (Rad/Sec)
1	1733.381
2	10863.698
3	30421.731

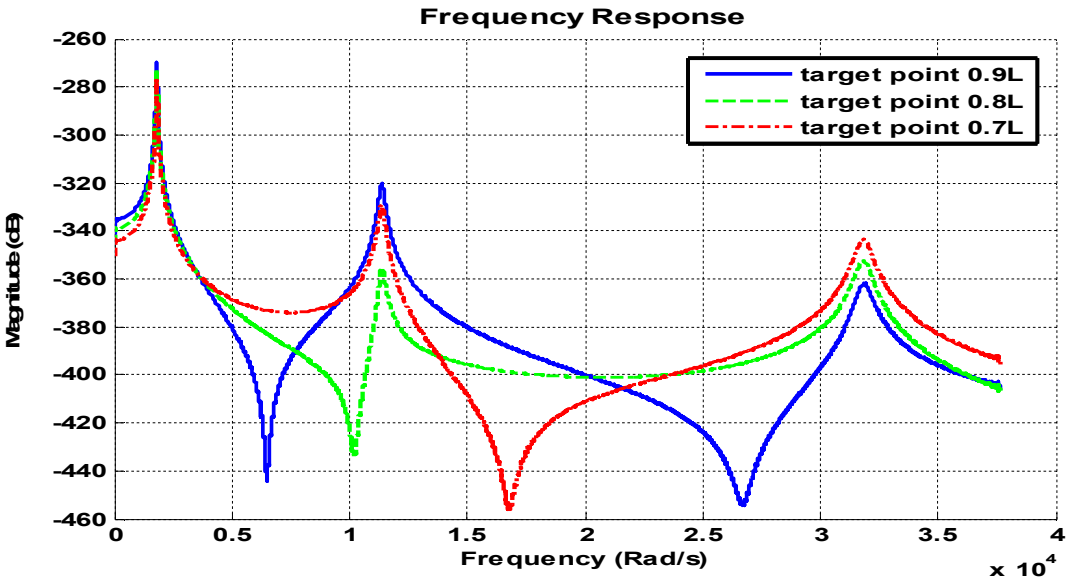

Fig. 8: Frequency response for different target points on the cantilever

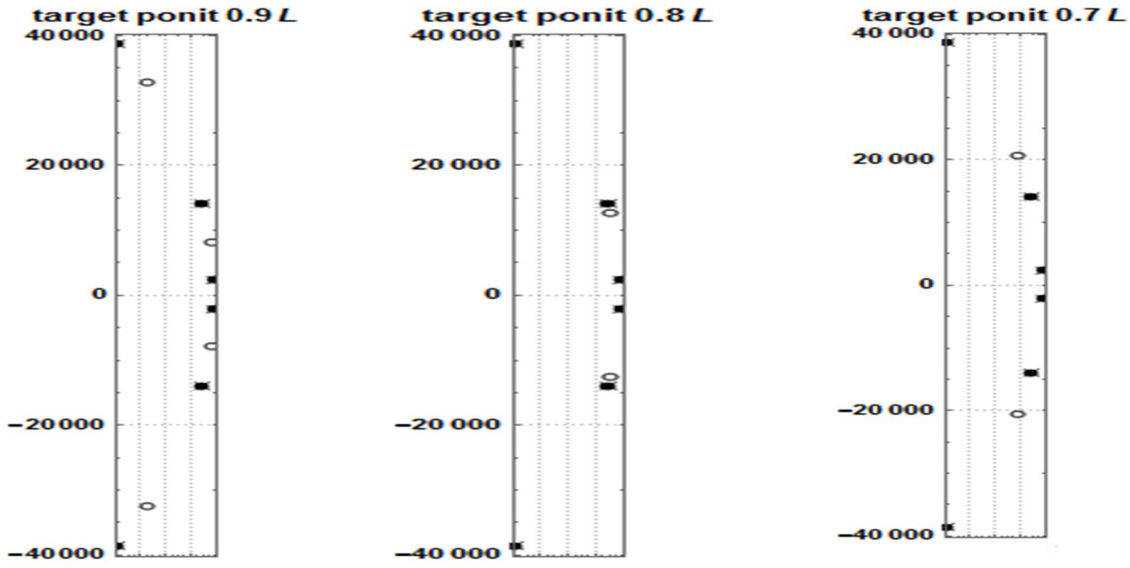

Fig. 9: Root locus diagram for different target points on the cantilever

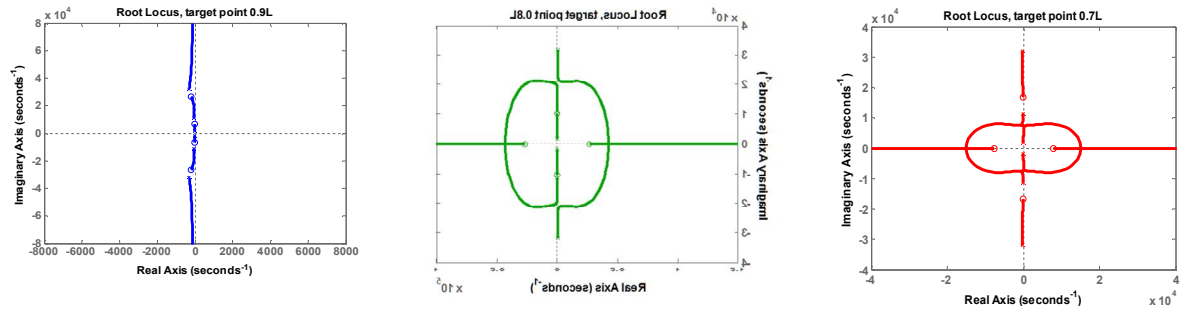

Fig. 10: Root locus diagrams for different target pints on the cantilever

As it is seen, at the target point $x = 0.9L$ both zeroes exist in the dynamic operation i.e. the system is minimum phase as was expected. But at the target point $x = 0.8L$ the second zero (zero between second and third poles) is eliminated and also at target point $x = 0.7L$, first zero (zero between first and second poles) is shifted and superseded the second zero. Neither at target point $x = 0.8L$, nor at $x = 0.7L$ is the system minimum phase because of the advent of RHP zeroes. It should be noted that the emergent of RHP zeroes due to changing the target point is an inherent feature of BPC actuators; hence, it's an inevitable phenomenon which has to be considered when aim is to design or utilizing a BPC actuator.

4. Experimental validation

In this section, an experimental setup is developed to validate the proposed dynamic model. For that, a laser sensor (ILD2300 made by Micro-Epsilon©) with a resolution of 10nm is utilized in the setup to measure the deflection of piezoelectric cantilever at different target points. Bimorph piezoelectric actuator (T215-A4-103X from Piezo System Company, Woburn, MA, USA) is clamped on one end and free at the other one where the free end is aligned across the laser's focus length. The geometric and material properties of the cantilever are listed in Table1. The cantilever is actuated by an applied voltage generated by a data acquisition card (PIC-1716, Advantech) and aplified by an aplifier (EPA-104-230). The data acquisition card (DAQ), with sampling rate of 250 kHz, also is used as an interface between laser and computer. Figure 11 shows the experimental set-up and configuration.

4.1. Linear dynamic identification

To identify the linear damping coefficients, an arbitrary target point, $l_t = 21.04\ mm = 0.88L$, was chosen for frequency response, and by fitting the simulation result on experimental result linear damping coefficient was attained in two steps.

First, in order to suppress the hysteresis and material nonlinearity effects, a chirp type input voltage with low-amplitude $0.2\ V$ was applied to the actuator and results were further analyzed as shown in Figure 12. Damping coefficients were obtained by fitting simulation results with experimental data for first and second mode shapes in both experiments. An acceptable consistency between experimental and simulation results could be seen and the obtained damping coefficients are provided in Table 1.

(a)

(b)

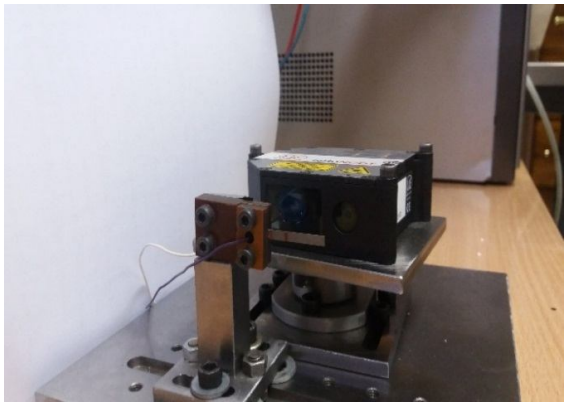

(c)

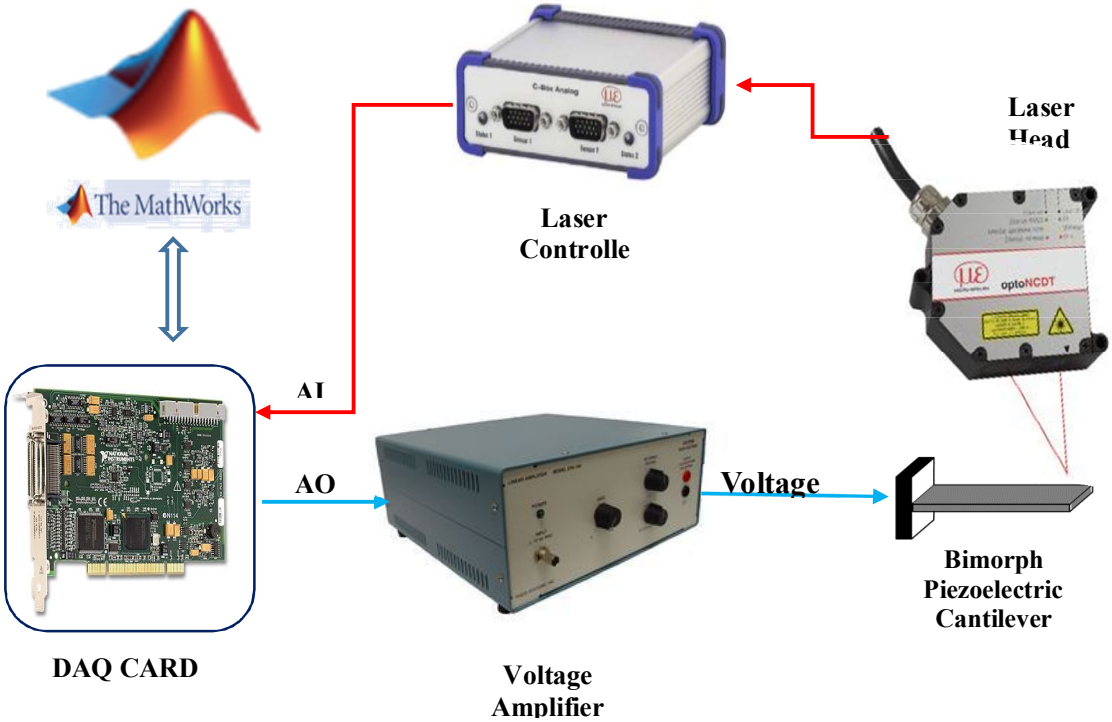

Fig. 11: Experimental setup (a, b) and configuration (c)

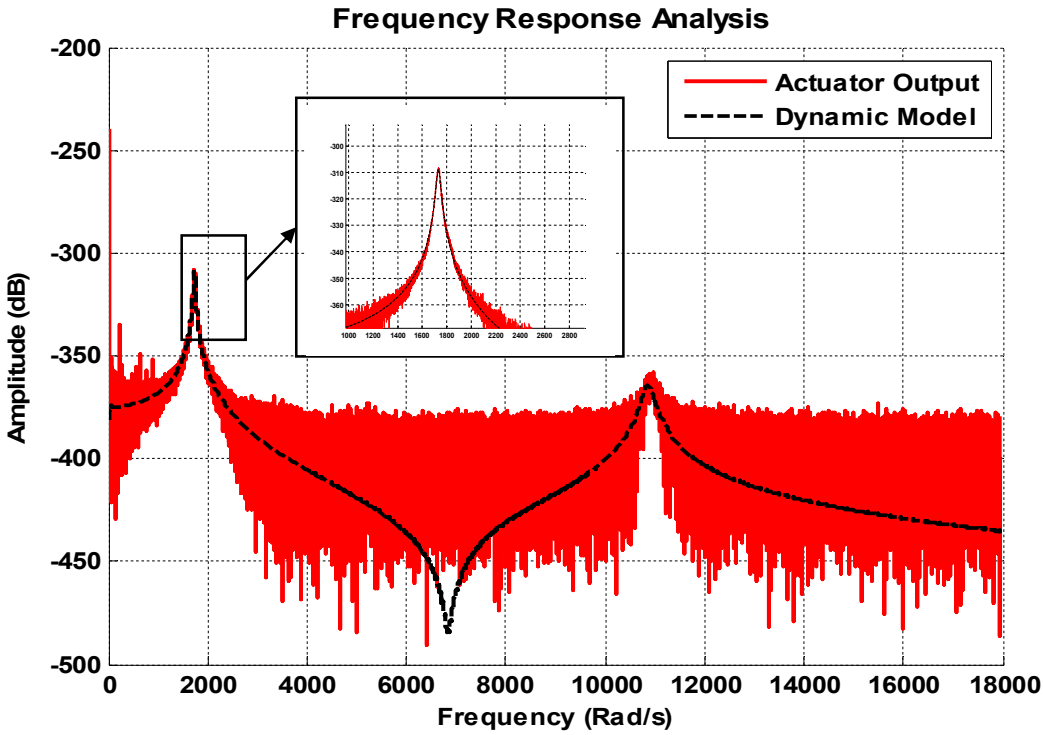

Fig. 12: *Frequency response for* $l_t = 21.04\,mm = 0.88L$ *and* $V = 0.2\,V$

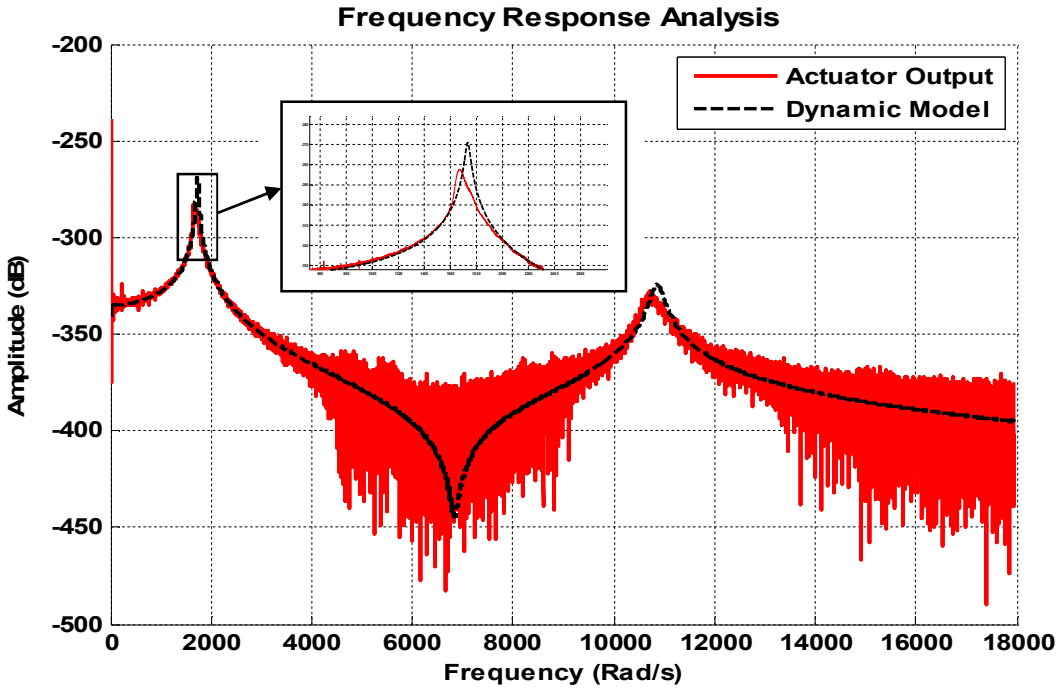

Fig. 13: Frequency response for $l_t = 21.04\,mm = 0.88L$ and $V = 2\,V$

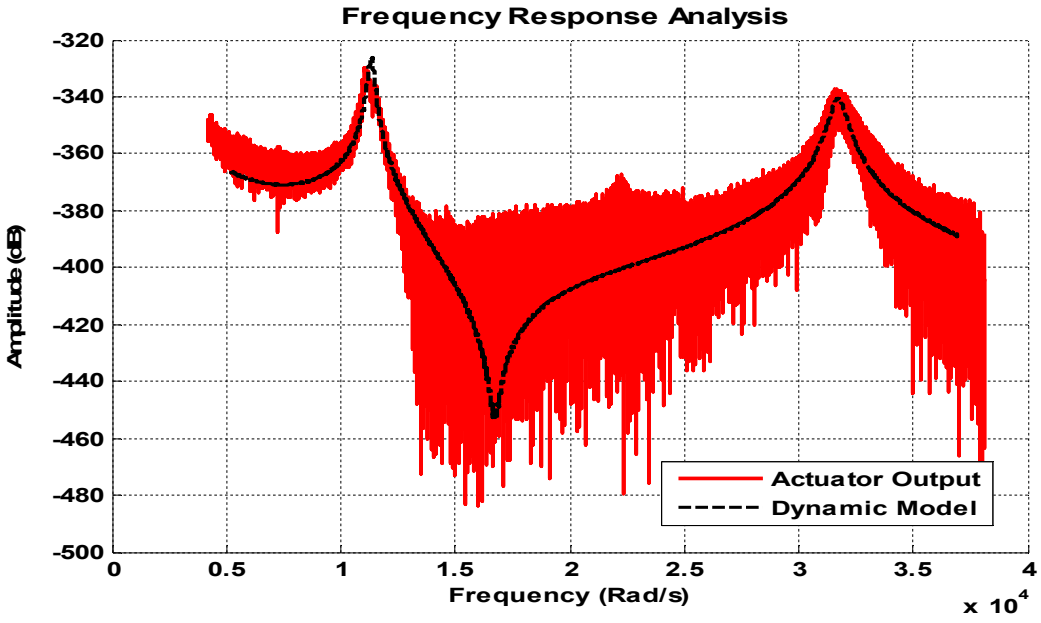

Fig. 14: Frequency response for $l_t = 17.98\,mm = 0.75L$ and $V = 2\,V$ frequency range = 600-6000 Hz

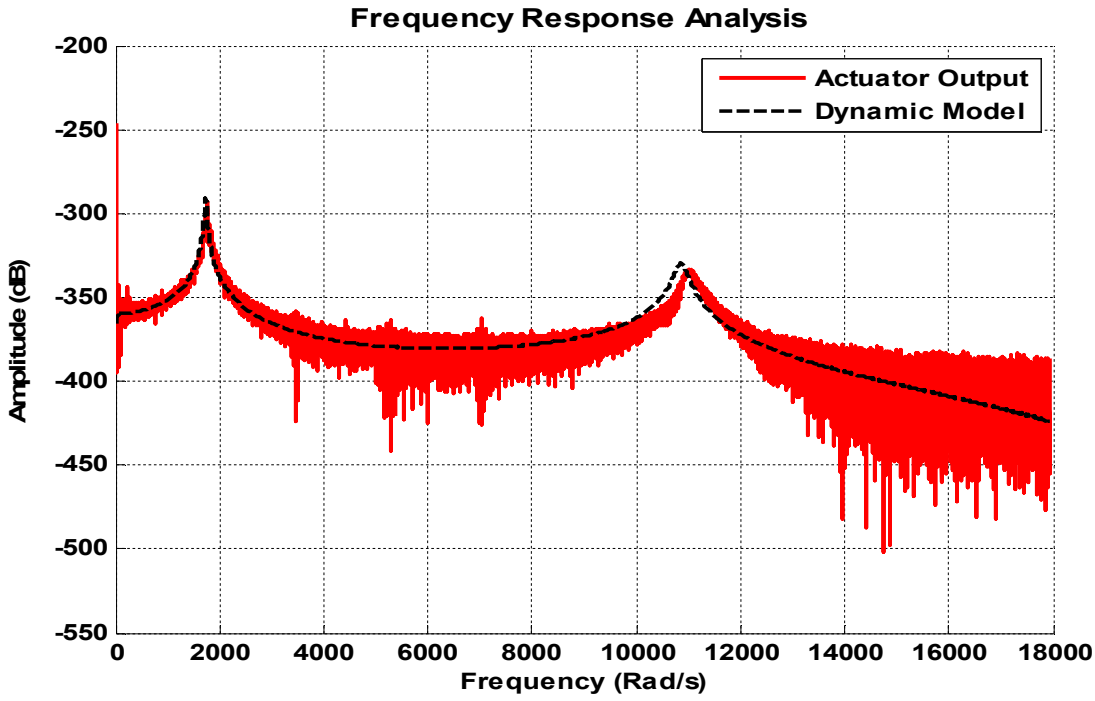

Fig. 15: Frequency response for $l_t = 14.77\,mm = 0.62L$ and $V = 1\,V$

(a)

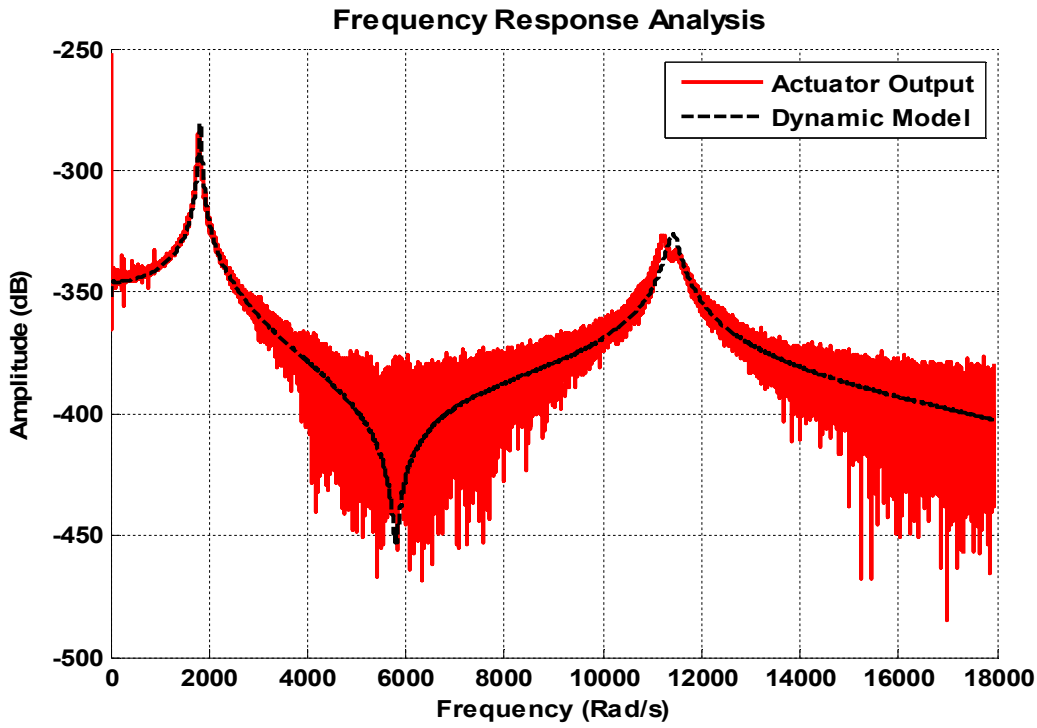

(b)

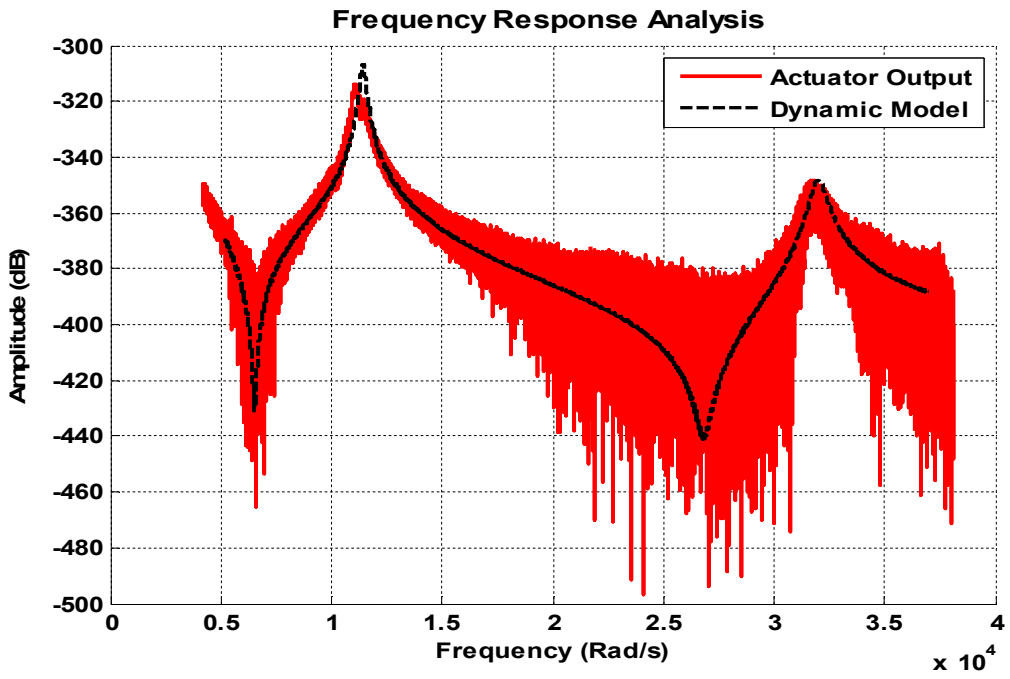

Fig. 16: Frequency response for $l_t = 21.58\ mm = 0.9$
(a): frequency range = 0-3000 Hz and input voltage = 1.4V
(b): frequency range = 600-6000 Hz and input voltage = 2V

(a)

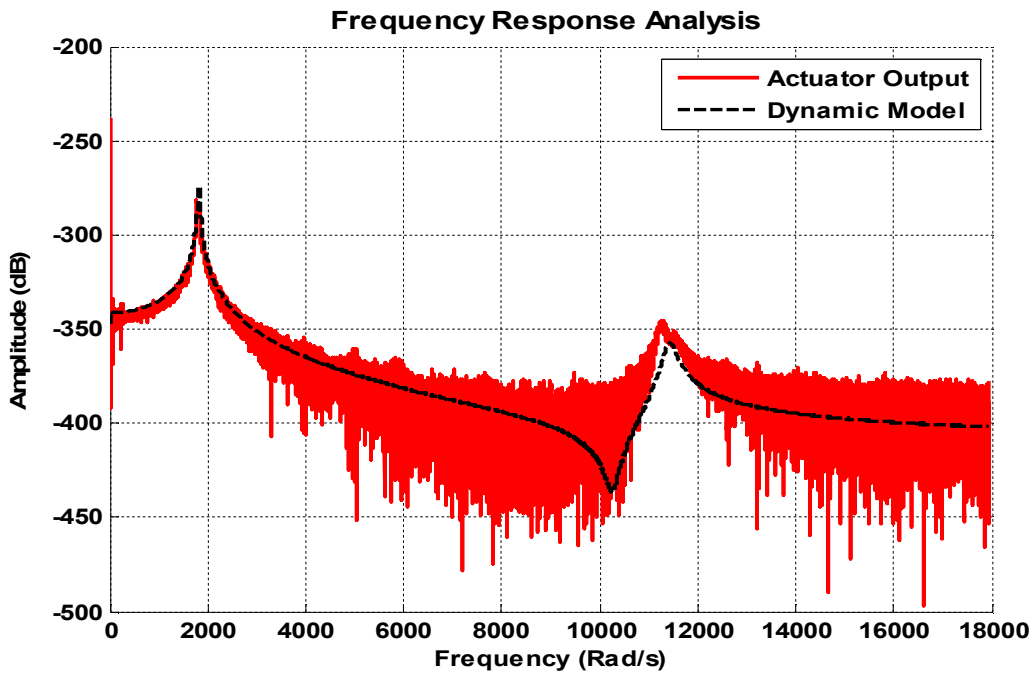

(b)

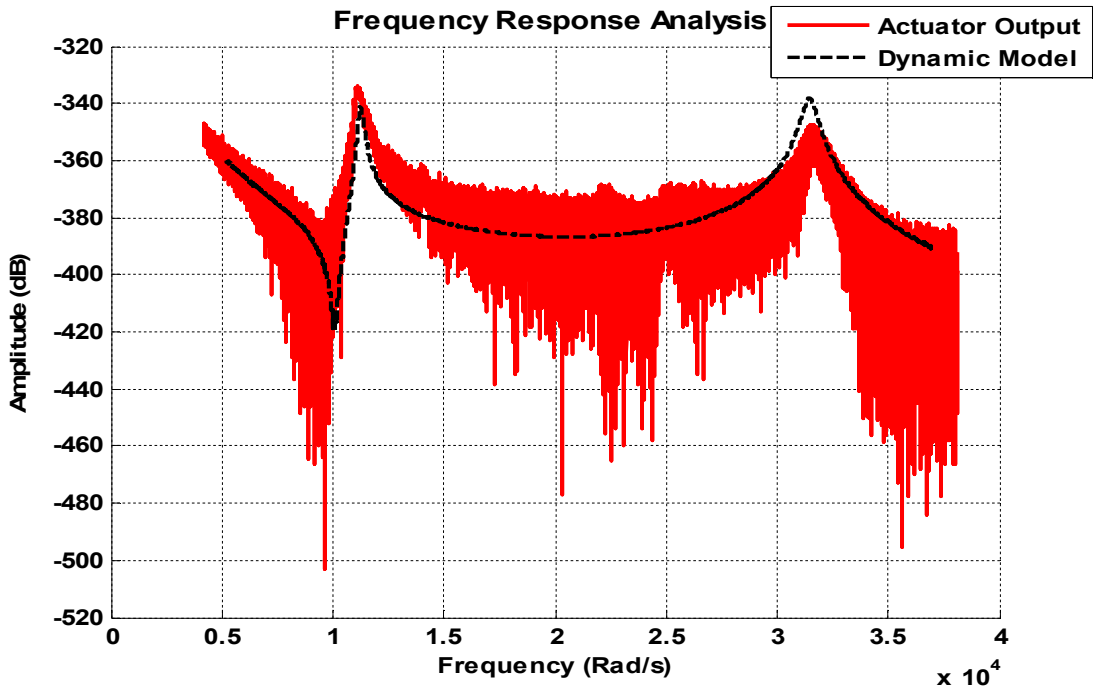

Fig. 17: Frequency response for $l_t = 19.18\ mm = 0.8$
(a): frequency range = 0-3000 Hz and input voltage = 1.4V
(b): frequency range = 600-6000 Hz and input voltage = 2V

(a)

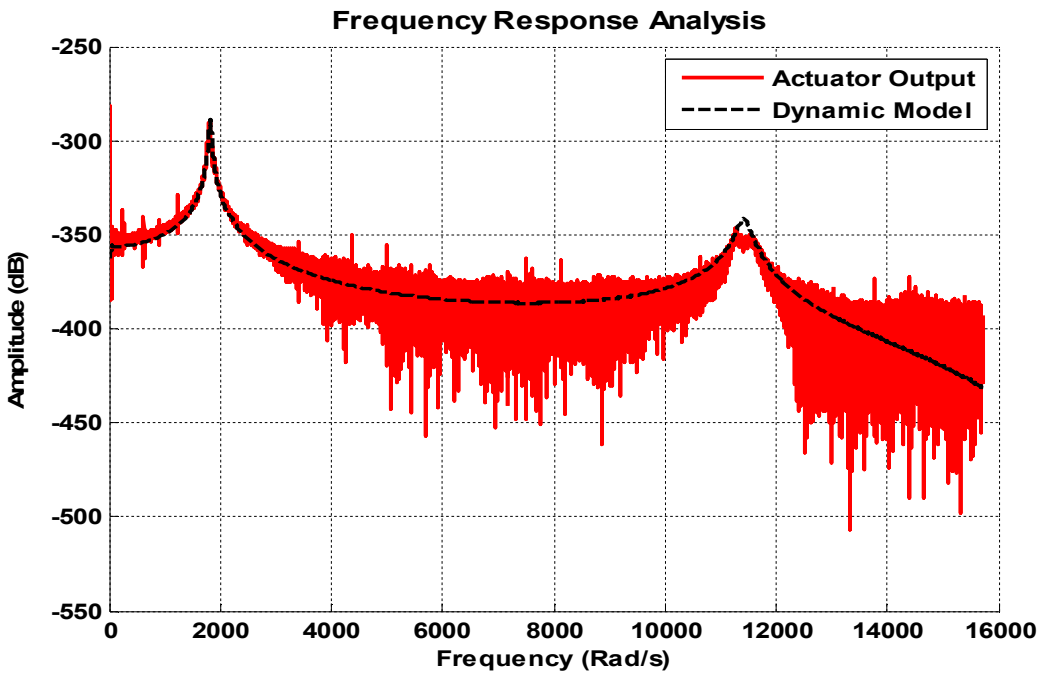

(b)

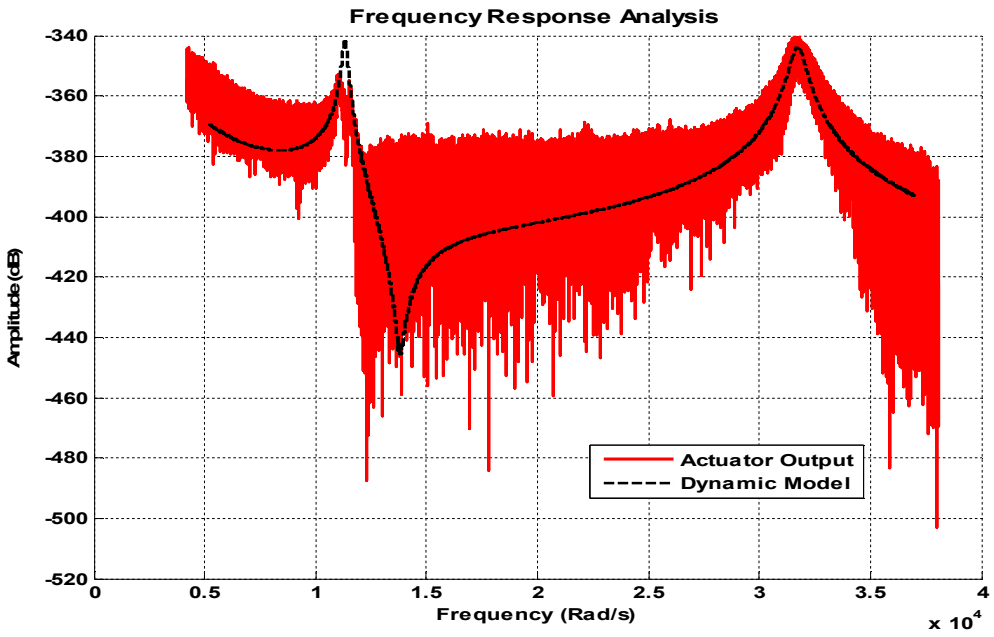

Fig. 18: Frequency response for $l_t = 16.78\ mm = 0.7$
(a): frequency range = 0-3000 Hz and input voltage = 1.4V
(b): frequency range = 600-6000 Hz and input voltage = 2V

It is notable that a distortion called softening can be seen around the natural frequencies by increasing the input voltage. It is caused by piezoelectric material nonlinearity which only happens near resonances and does not affect the general actuator response [32-34].

To evaluate the identification results, proposed dynamic model with identified damping coefficients was applied to two target points, $l_t = 0.62L$ and $l_t = 0.75L$, at different frequencies and the results are compared with experimental results. As it is seen from Figures 14, 15, an acceptable consistency between the results approves the validity of identification section.

Second, to illustrate the zero effect it is necessary to increase the amplitude of input voltage. In this regard, the amplitude of chirp type input voltage was $2\,V$ and the experiment results are depicted in Figure 13.

4.2. Dynamic behavior analysis

To investigate zero-elimination phenomenon experimentally, frequency response of three different target points, $\mathrm{l_t} = 0.9L$, $\mathrm{l_t} = 0.8L$, and $\mathrm{l_t} = 0.7L$, are investigated. Results are depicted in Figures 16, 17 and Figure 18, respectively. It is seen that position of zeroes change by changing the target point's position according to the fixed position of poles. Moreover, based on the results in section 3.2, it is expected to observe the system operating in non-minimum phase region both at $\mathrm{l_t} = 0.8L$ and $\mathrm{l_t} = 0.7L$ due to the elimination of the second and first zeros, respectively. This expectation is validated by experimental results in this section. In each figure, frequency responses of experimental results are shown along with the results of proposed dynamic model and a good consistency is seen between them. It should be noted that in each case the actuator underwent two different range of frequencies, first = *0-3000 Hz* and second = *600-6000 Hz,* to cover all first three vibrational modes. The second frequency range was done with a greater amplitude of input voltage to better show the zero-elimination effect.

5. Conclusion

In this paper, a continuous model for BPC actuator's dynamic behavior has been developed considering both transverse and longitudinal vibrations. Modal analysis was utilized for discretizing coupled set of vibration equations which resulted in uncoupled equations only for fully covered BPC actuator on both sides. Furthermore, dynamic behavior was analyzed to determine the exact non-minimum phase region along the actuator's length. A simulation study was employed to better clarify zero-elimination phenomenon based on non-minimum phase concept considering first three vibrational modes for different target points. The proposed dynamic model was evaluated experimentally, and adequate consistency with theoretical results confirmed the validity of proposed model.

Acknowledgments

The authors are indebted to NTRC (New Technology Research Center) of Amirkabir University of Technology (Tehran Polytechnic) for providing the resources and facilities for this research.

References

[1] M. Motamedi, M.T. Ahmadian, G. Vossoughi, S.M. Rezaei, M. Zareinejad, Adaptive sliding mode control of a piezo-actuated bilateral teleoperated micromanipulation system, Precision Engineering, 35 (2011) 309-317.
[2] T. Müller, A. Kugi, G. Bachmaier, M. Gerlich, Modelling and identification of a piezoelectrically driven fuel injection control valve, Mathematical and Computer Modelling of Dynamical Systems, 16 (2010) 285-305.

[3] S. Shim, M.G. Kim, K. Jo, Y.S. Kang, B. Lee, S. Yang, S.-M. Shin, J.-H. Lee, Dynamic characterization of human breast cancer cells using a piezoresistive microcantilever, Journal of biomechanical engineering, 132 (2010) 104501.
[4] Q. Xu, Precision position/force interaction control of a piezoelectric multimorph microgripper for microassembly, IEEE Transactions on Automation Science and Engineering, 10 (2013) 503-514.
[5] S. Bashash, R. Saeidpourazar, N. Jalili, Development, analysis and control of a high-speed laser-free atomic force microscope, Review of Scientific Instruments, 81 (2010) 023707.
[6] A. Salehi-Khojin, S. Bashash, N. Jalili, Modeling and experimental vibration analysis of nanomechanical cantilever active probes, Journal of Micromechanics and Microengineering, 18 (2008).
[7] N. Garcia, Theory of scanning tunneling microscopy and spectroscopy: resolution, image and field states, and thin oxide layers, IBM journal of research and development, 30 (1986) 533-542.
[8] M. Mohammadpour, M. Dardel, M.H. Ghasemi, M.H. Pashaei, Nonlinear energy harvesting through a multimodal electro-mechanical system, Journal of Theoretical and Applied Vibration and Acoustics, 1 (2015) 73-84.
[9] R. Toscano, I.A. Ivan, Robust structured controllers for piezoelectric microactuators, ISA transactions, 53 (2014) 1857-1864.
[10] W.M. Chen, T.S. Liu, Modeling and experimental validation of new two degree-of-freedom piezoelectric actuators, Mechatronics, 23 (2013) 1163-1170.
[11] I.A. Ivan, M. Rakotondrabe, P. Lutz, N. Chaillet, Quasistatic displacement self-sensing method for cantilevered piezoelectric actuators, Review of Scientific instruments, 80 (2009) 065102.
[12] O. Bilgen, M.A. Karami, D.J. Inman, M.I. Friswell, The actuation characterization of cantilevered unimorph beams with single crystal piezoelectric materials, Smart Materials and Structures, 20 (2011) 055024.
[13] S.-N. Chen, G.-J. Wang, M.-C. Chien, Analytical modeling of piezoelectric vibration-induced micro power generator, Mechatronics, 16 (2006) 379-387.
[14] G. Wang, Analysis of bimorph piezoelectric beam energy harvesters using Timoshenko and Euler–Bernoulli beam theory, Journal of Intelligent Material Systems and Structures, 24 (2013) 226-239.
[15] S. Peng, X. Zheng, J. Sun, Y. Zhang, L. Zhou, J. Zhao, S. Deng, M. Cao, W. Xiong, K. Peng, Modeling of a micro-cantilevered piezo-actuator considering the buffer layer and electrodes, Journal of Micromechanics and Microengineering, 22 (2012) 065005.
[16] S. Gorthi, A. Mohanty, A. Chatterjee, Cantilever beam electrostatic MEMS actuators beyond pull-in, Journal of Micromechanics and Microengineering, 16 (2006) 1800.
[17] M. Vagia, A frequency independent approximation and a sliding mode control scheme for a system of a micro-cantilever beam, ISA transactions, 51 (2012) 325-332.
[18] J. Yi, S. Chang, Y. Shen, Disturbance-observer-based hysteresis compensation for piezoelectric actuators, IEEE/Asme transactions on mechatronics, 14 (2009) 456-464.
[19] P.-P. Chao, P.-Y. Liao, M.-Y. Tsai, C.-T. Lin, Robust control design for precision positioning of a generic piezoelectric system with consideration of microscopic hysteresis effects, Microsystem technologies, 17 (2011) 1009-1023.
[20] H. Ghafarirad, S.M. Rezaei, A.A.D. Sarhan, M. Zareinejad, Continuous dynamic modelling of bimorph piezoelectric cantilevered actuators considering hysteresis effect and dynamic behaviour analysis, Mathematical and Computer Modelling of Dynamical Systems, 21 (2015) 130-152.
[21] A.A. Tahmasebi Moradi, S. Ziaei-Rad, R. Tikani, H.R. Mirdamadi, A finite element model for extension and shear modes of piezo-laminated beams based on von Karman's nonlinear displacement-strain relation, Journal of Theoretical and Applied Vibration and Acoustics, 2 (2016) 35-64.
[22] N. Jalili, Piezoelectric-Based Systems Modeling, in: Piezoelectric-Based Vibration Control, Springer, 2010, pp. 183-232.
[23] S.S. Rao, Vibration of continuous systems, John Wiley & Sons, 2007.
[24] B. Engquist, A.-K. Tornberg, R. Tsai, Discretization of Dirac delta functions in level set methods, Journal of Computational Physics, 207 (2005) 28-51.
[25] A. Erturk, Assumed-modes modeling of piezoelectric energy harvesters: Euler–Bernoulli, Rayleigh, and Timoshenko models with axial deformations, Computers & Structures, 106 (2012) 214-227.
[26] S. Basak, A. Raman, S.V. Garimella, Dynamic response optimization of piezoelectrically excited thin resonant beams, Journal of vibration and acoustics, 127 (2005) 18-27.
[27] S. Yu, S. He, W. Li, Theoretical and experimental studies of beam bimorph piezoelectric power harvesters, Journal of Mechanics of Materials and Structures, 5 (2010) 427-445.

[28] A. Erturk, D.J. Inman, A distributed parameter electromechanical model for cantilevered piezoelectric energy harvesters, Journal of vibration and acoustics, 130 (2008) 041002.
[29] A. Erturk, D.J. Inman, On mechanical modeling of cantilevered piezoelectric vibration energy harvesters, Journal of Intelligent Material Systems and Structures, 19 (2008) 1311-1325.
[30] H.K. Khalil, Nonlinear Systems. 3rd Prentice-Hall, Upper Saddle River, NJ, (2002).
[31] K. Ogata, Modern control engineering 5th edition. Lugar: Upper Saddle River, New Jersey 07458, Ed: Prentice Hall, (2009) 55.
[32] S.C. Stanton, A. Erturk, B.P. Mann, D.J. Inman, Nonlinear piezoelectricity in electroelastic energy harvesters: Modeling and experimental identification, Journal of Applied Physics, 108 (2010) 074903.
[33] S.C. Stanton, A. Erturk, B.P. Mann, D.J. Inman, Resonant manifestation of intrinsic nonlinearity within electroelastic micropower generators, Applied Physics Letters, 97 (2010) 254101.
[34] M. Daqaq, N. Jalili, S.N. Mahmoodi, Nonlinear Dynamics of A Piezoelectrically-actuated Microcantilever Sensor, in: ENOC-2008, Saint Petersburg, Russia, 2008.